4. RESULTS OF OQUIRRH FAULT IMAGING

4.1 Reflection Results

Figure 28 shows the final migrated section with the horizontal axis in CMP number and the vertical axis in depth. This section shows four shallow horizons that are offset by an antithetic fault near CMP 100 and can be correlated across this fault. The horizons are coherent through the central portion of the fault graben between the main Oquirrh fault and the antithetic fault. The horizons are then truncated by the main Oquirrh fault at CMP 580 and are difficult to correlate into the hanging wall, east of the main fault. This may be attributed to a large zone of deformation associated with movement on the fault. Also, the deposition rate in the footwall is greater than in the hanging wall as the main fault marks the transition from the Oquirrh Mountains to the Tooele Valley (Soloman, 1996). This produces thicker sequences of Quaternary fill in the footwall that are more easily mapped with the seismic reflection technique.

In the footwall, the reflection horizons are coherent and horizontal until CMP 350 where horizons 2, 3, and 4 become synclinal in shape and extend to CMP 305. This may be due to a depositional facies change as in this region the shallow geology moves from colluvial deposits to eolian and colluvial deposits as shown in the trench cross-section (see Figure 29). From CMP 300 to CMP 200 the horizons are fairly flat. At CMP 200 the horizons begin to slope gently to the West, toward the antithetic fault. At CMP 100 all four horizons are offset by the antithetic fault. The dip angles on the main fault and the antithetic fault are estimated from the migrated section to be $85° \pm 10°$ and $75° \pm 10°$, respectively. This is consistent with the 85° dip angle estimated in a trench study (Olig et al., 1996) along the main fault.

The four horizons in the vicinity of the antithetic fault begin to dip down to the

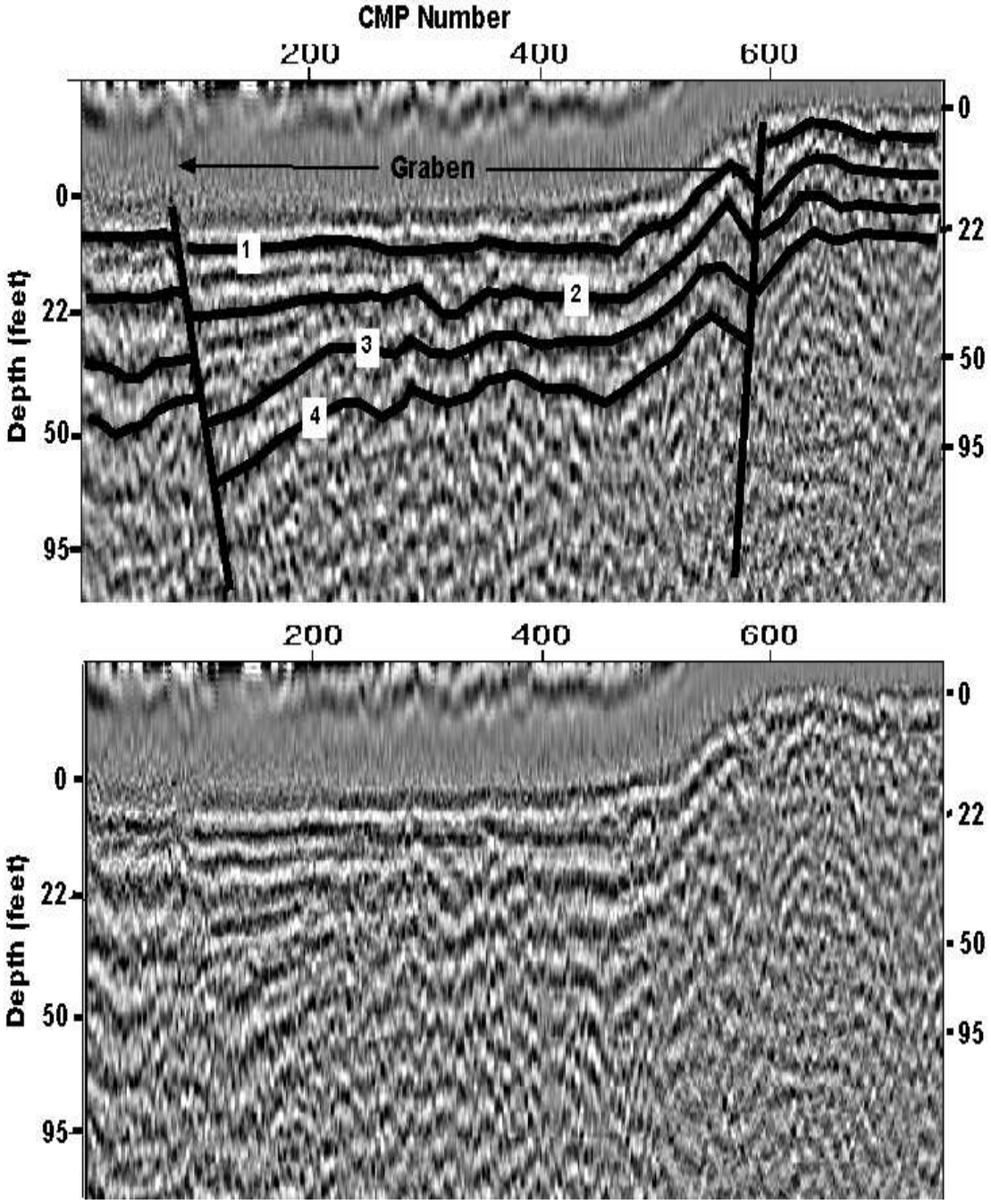

Figure 28: The final migrated section with the horizontal axis in CMP and the vertical axis in depth.

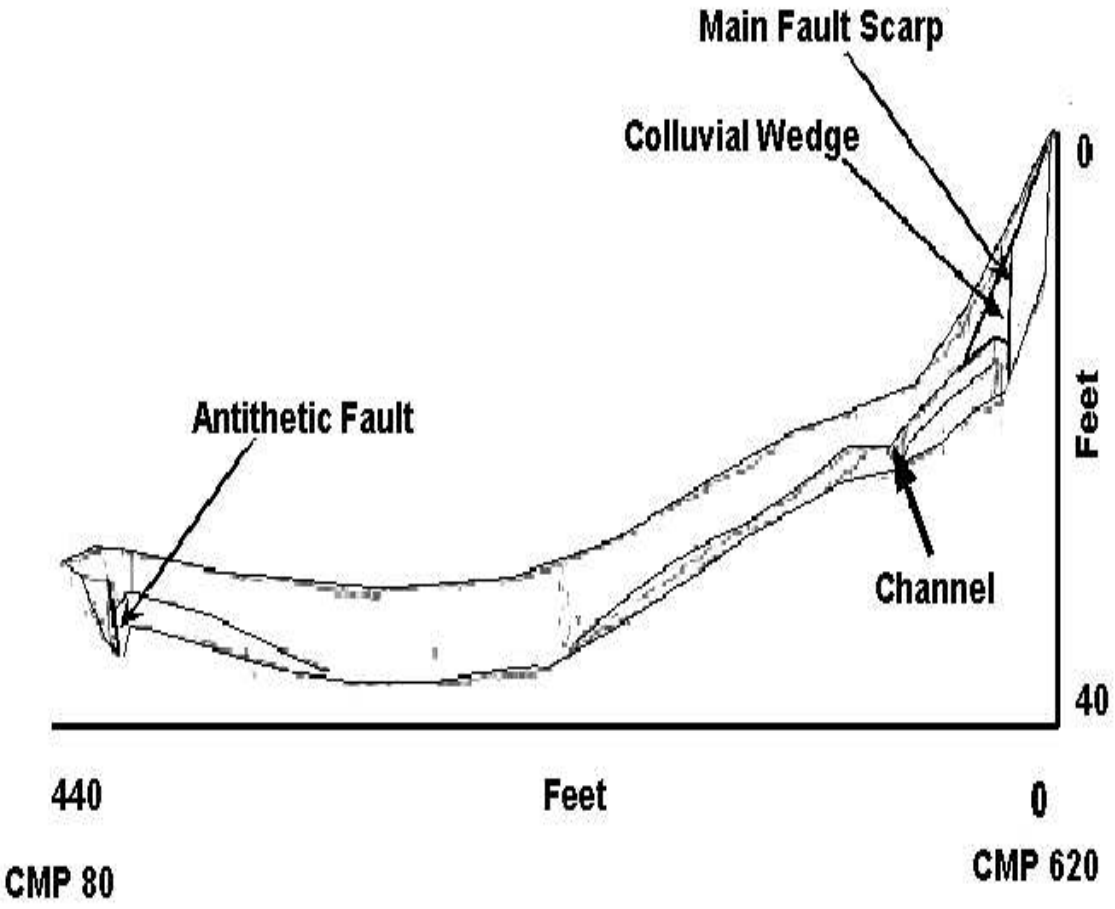

Figure 29: Simplified cross-section from trench BC-3, after Olig et al. (1996). The vertical exaggeration is 6.5:1.

west as they approach the antithetic fault. The amount of dip increases with greater depth from horizon 1 to horizon 4. Also, the thickness of the layers separating the horizons increases as the horizons approach the antithetic fault. The amount of thickening also increases with increasing depth. The layer separating horizons 3 and 4 exhibits more thickening than the layer separating horizons 2 and 3 and the layer separating horizons 1 and 2 exhibits the least amount of thickening. Figure 30 shows a portion of the stacked section in the vicinity of the antithetic fault. This structure looks very similar to growth fault sequences seen in the Gulf of Mexico on seismic data and to seismic mapping of the Wasatch fault, Utah (Smith and Bruhn, 1984). Also, as horizons 1 and 2 approach the antithetic fault an additional horizon becomes apparent just below both horizons. These horizons produce a wedge-shaped structure that is directly adjacent to the antithetic fault. Similar features are noticed adjacent to the main fault below horizons 1 and 2 but are more subtle. These features might be colluvial wedges, but this interpretation is not unambiguous.

The results of reflection imaging are compared with a common offset gather for an offset of 30 feet. Figure 31 shows both the common offset gather and the final stacked section. This type of analysis adds confidence to the reflection image as both images display similar character. The common offset gather displays an offset in the first arrival that is associated with the antithetic fault seen in the final stacked section. A velocity increase is evident by a "pull-up" in the first arrival at the center of the common offset gather, this feature is also seen in the final stacked section near the center of the image at CMP 380. The synclinal structure seen near CMP 350 in the stacked section is also recognized in the common offset gather.

4.2 Tomography Results

A 3-D velocity tomogram is inverted from 83,570 traveltimes and is shown in Figure 32. This tomogram clearly delineates the colluvial wedge associated with the most recent surface rupturing event on the Oquirrh fault, and the colluvial wedge image correlates well with the actual wedge location mapped in the geologic cross-section. This correlation is shown in Figure 33 which is a comparison of the geologic

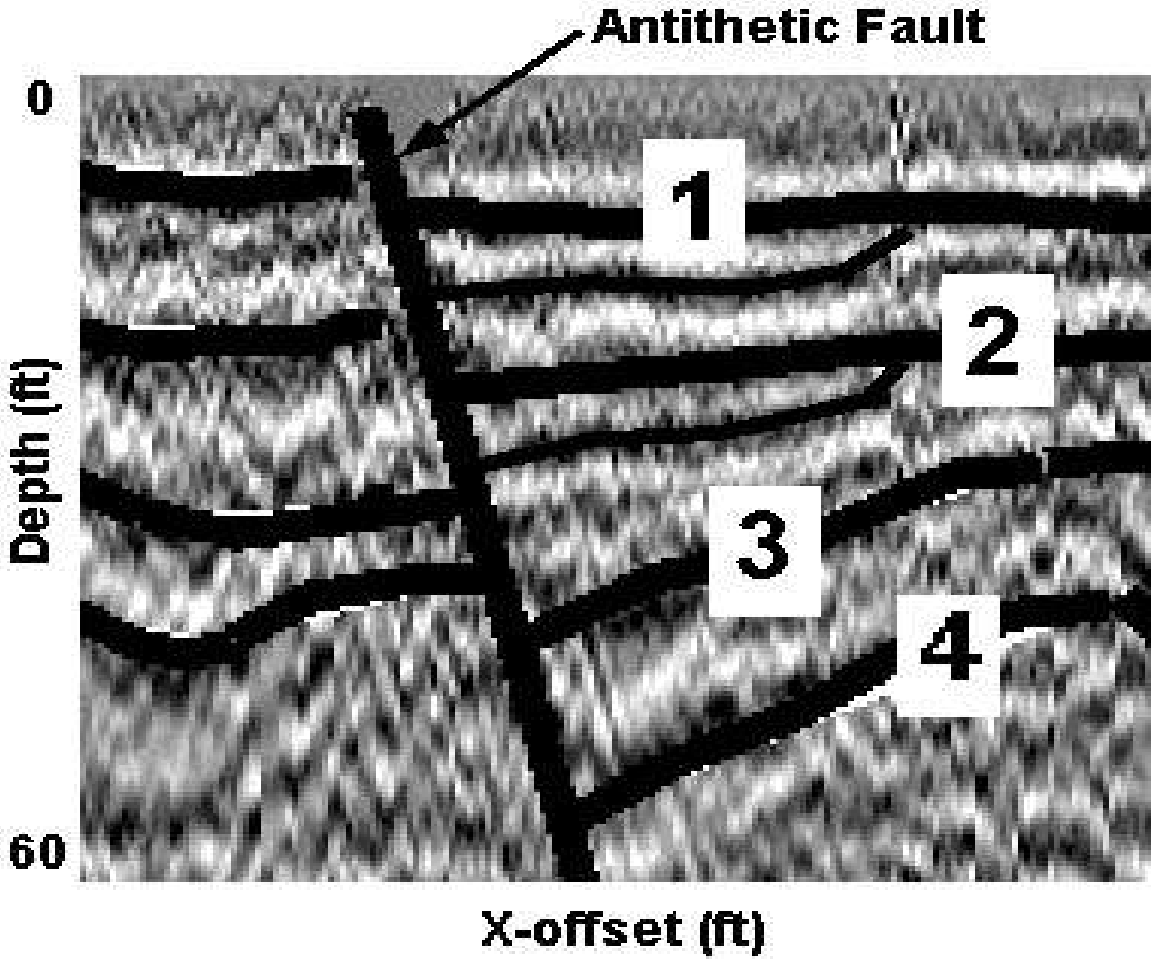

Figure 30: Zoom view of the reflectivity image of the antithetic fault. Notice the thickening and sloping of horizons 1-4 as they approach the antithetic fault.

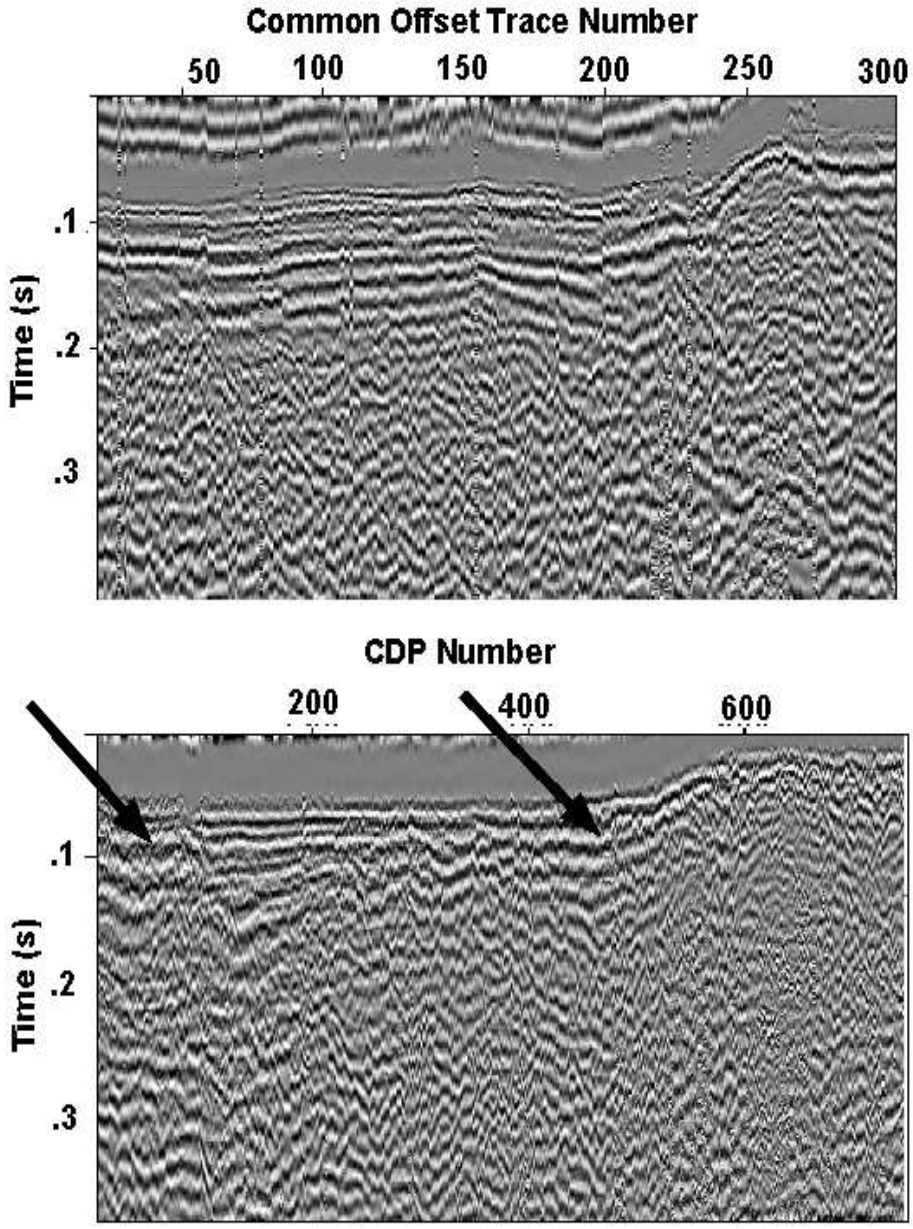

Figure 31: Common offset gather for an offset of 30 ft and the final stacked section, where the times in the common offset gather have been adjusted for topography. Key features are indicated by arrows and described in the text.

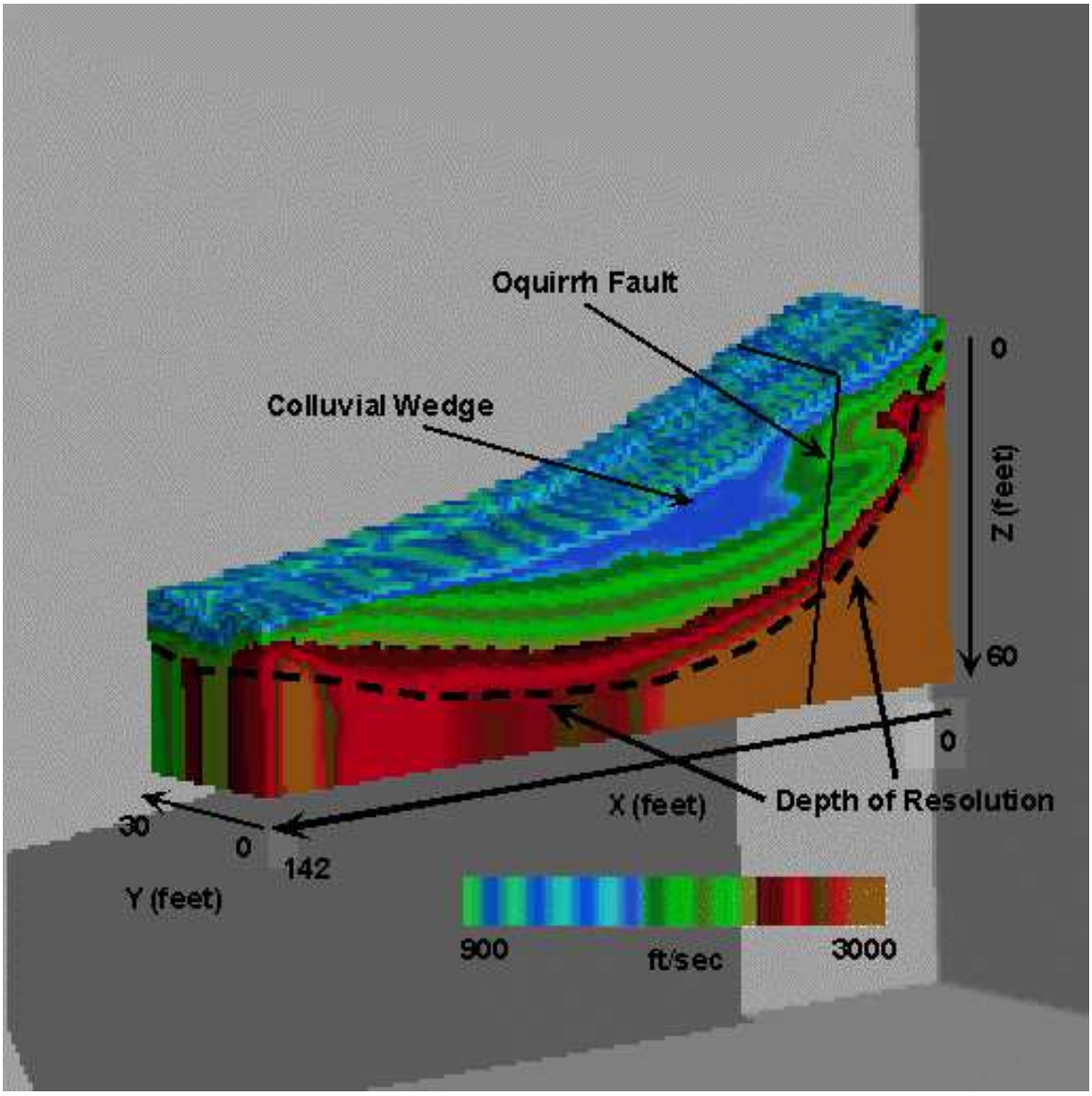

Figure 32: 3-D velocity tomogram computed from the traveltimes picked from the 3-D data. Note the wedge shaped low velocity region associated with the colluvial wedge.

cross-section and the equivalent portion of the 3-D tomogram.

Figure 34 reveals a channel running parallel to the main fault, where both the channel and the colluvial wedge are identified by low-velocity zones (LVZ's) in the 3-D tomogram. Here a velocity depression is located at about X=60 ft (LVZ 1) and is parallel to the fault scarp. Another velocity depression is located at about X=105 ft (LVZ 2). The large gradient located at about X=120 ft is interpreted to represent the buried fault scarp where the geology changes from undeformed sediments into a rapidly deposited colluvial wedge that produces a velocity low. An independent piece of evidence that verifies the velocity low recognized in the tomogram is a semblance analysis of CMP gathers over the colluvial wedge. The velocity depression at X=60 ft is a shallow channel that correlates well with the channel shown in Figure 29.

Figure 35 shows an X-Z slice taken from the 3-D tomogram at Y=10 ft. The shape of the colluvial wedge is delineated by the wedge shaped low-velocity region located near (X,Z)=(105 ft,17 ft). Figures 36 and 37 show X-Z slices of the 3-D tomogram at Y=15 ft and Y=20 ft, respectively. These images also delineate a similarly shaped colluvial wedge in the same area identified in Figure 35.

Figure 38 shows a 2-D tomogram, where the 2-D tomogram is constructed by inverting just the inline traveltimes along an E-W slice of the 3-D data. The images obtained from 2-D and 3-D tomography are comparable and have many similar features. The 3-D tomograms show additional features in the vicinity of the main fault. For example, a low velocity zone (LVZ 2 in Figure 34) adjacent to the fault scarp is revealed in the 3-D tomogram but is not seen in the 2-D tomogram. This is significant because LVZ 2 is associated with the colluvial wedge and is the most important feature identified in the 3-D tomogram.

Viewing the raypaths calculated for this model can help define regions in the result that are reliable. Figure 39 shows the areas in the model that were visited by at least 500 rays. Here we see many cells being well visited at dpeths down to 40 ft. Dueker et al. (1993) defines cells that have been visited by at least 3 rays as reliable for crustal scale tomography.

Figure 40 shows a portion of the stacked section that coincides with the 3-D

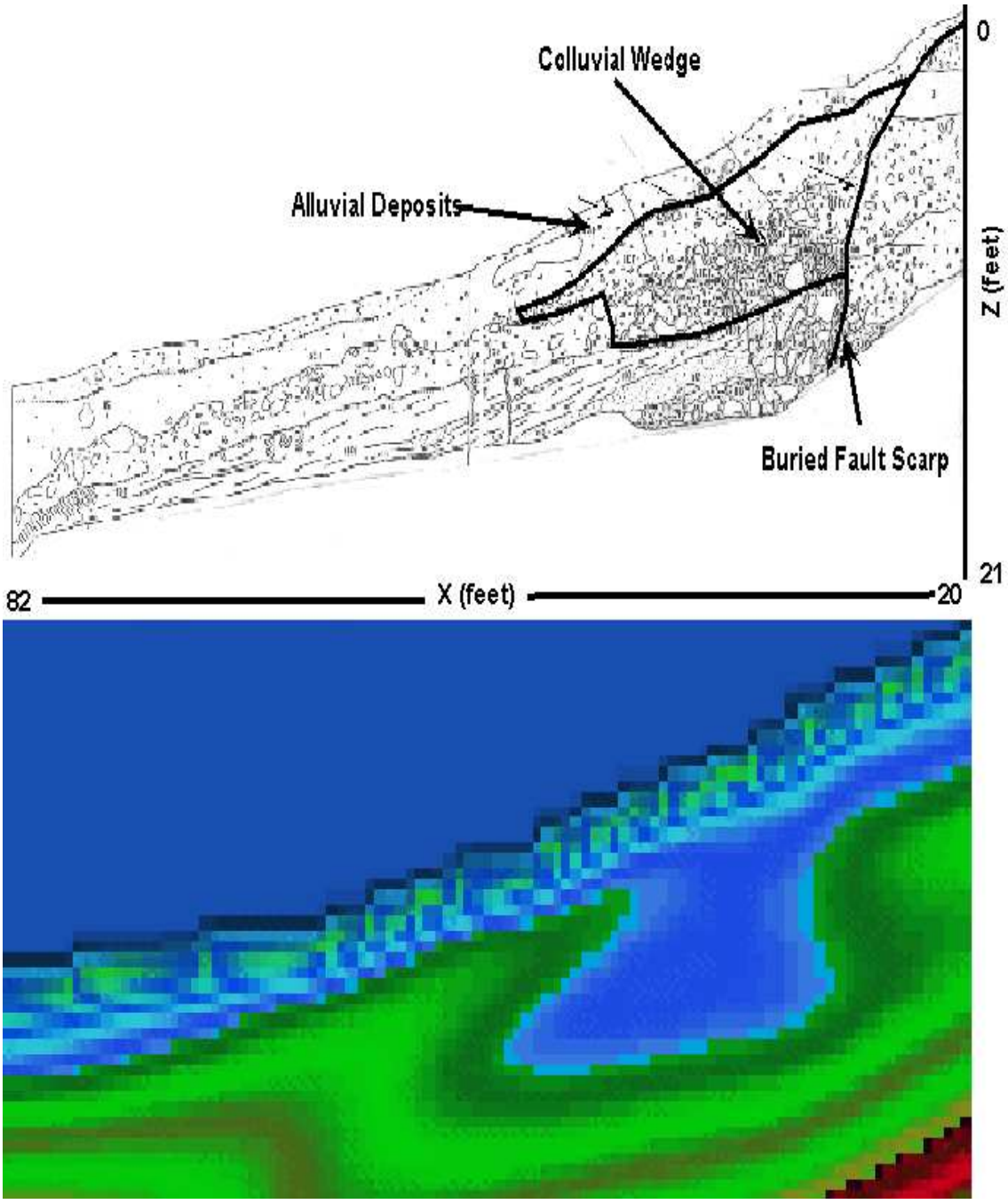

Figure 33: Comparison of the geologic cross-section (Olig et al., 1996) and the equivalent portion of the 3-D tomogram. Notice the strong correlation between both figures in the location and shape of the colluvial wedge.

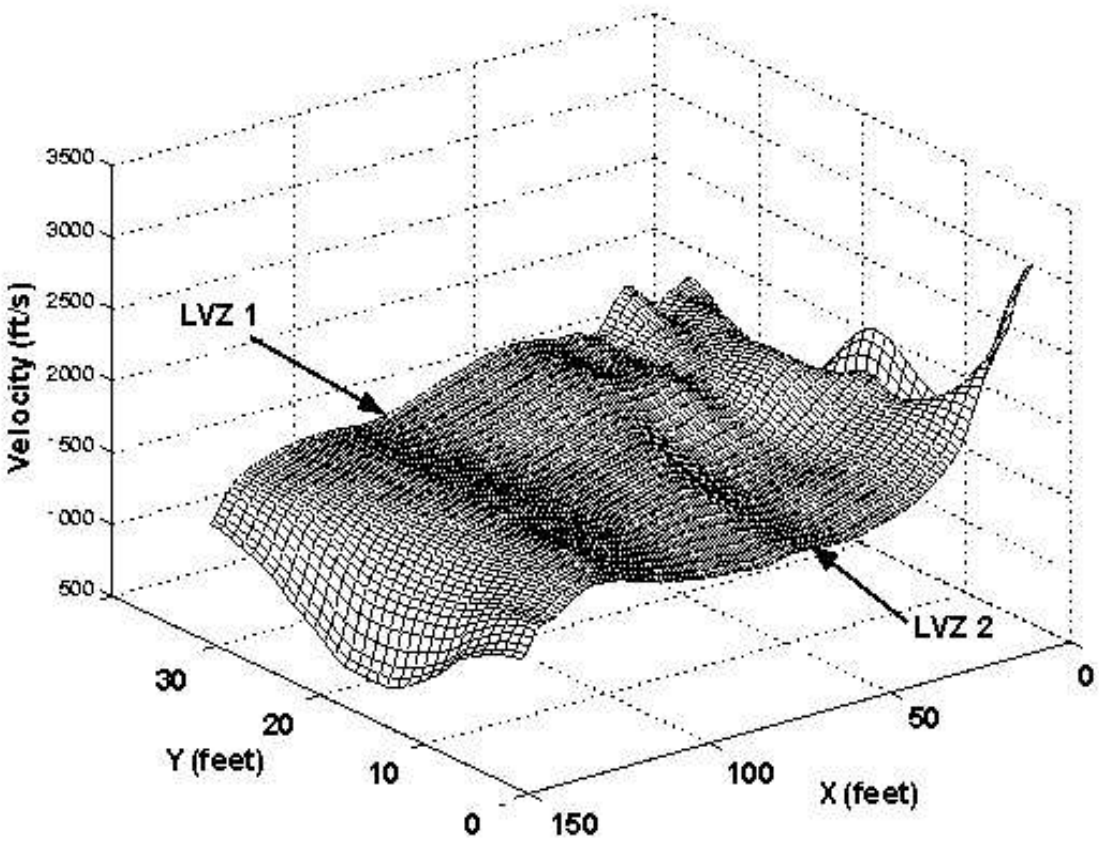

Figure 34: Horizontal slice of 3-D tomogram at Z=33 ft. Notice the velocity depression (LVZ 2) that r5uns parallel to the fault and the velocity depression LVZ 1 that corresponds to the colluvial wedge. LVZ 2 is interpreted in the trench log as a channel.

survey area and a slice of the 3-D tomogram, where the slice is coincident with the 2-D seismic line. This figure shows an ambiguous correlation between the reflection and tomography results in the location of the main fault and the colluvial wedge. The reflection section does not clearly image the colluvial wedge, but the tomographic image clearly delineates its geometry. Without the 3-D tomogram identification of the presence, location, and geometry of the colluvial wedge is ambiguous.

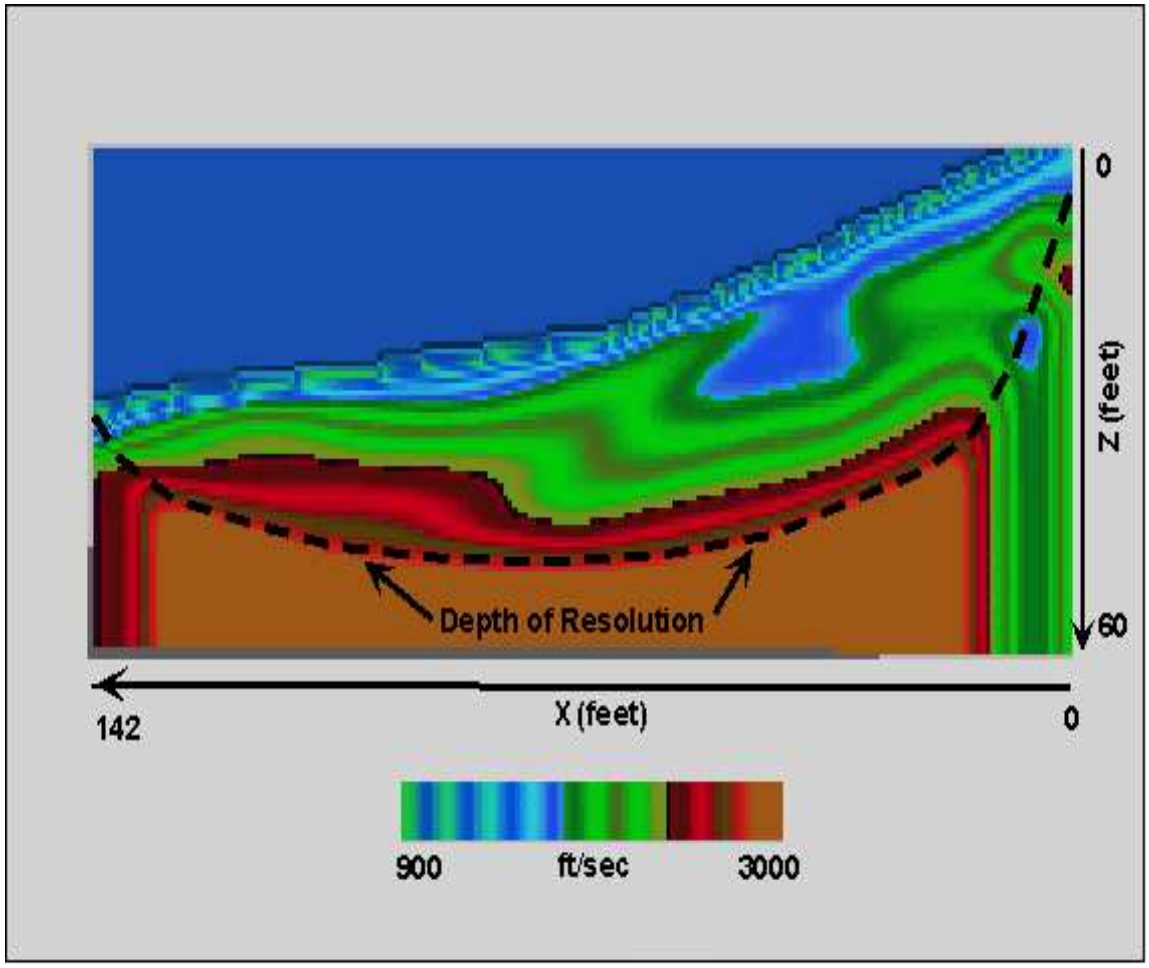

Figure 35: X-Z slice of the 3-D velocity tomogram sliced at y=10 ft. The colluvial wedge is clearly identified in the figure and is characterized by a low velocity.

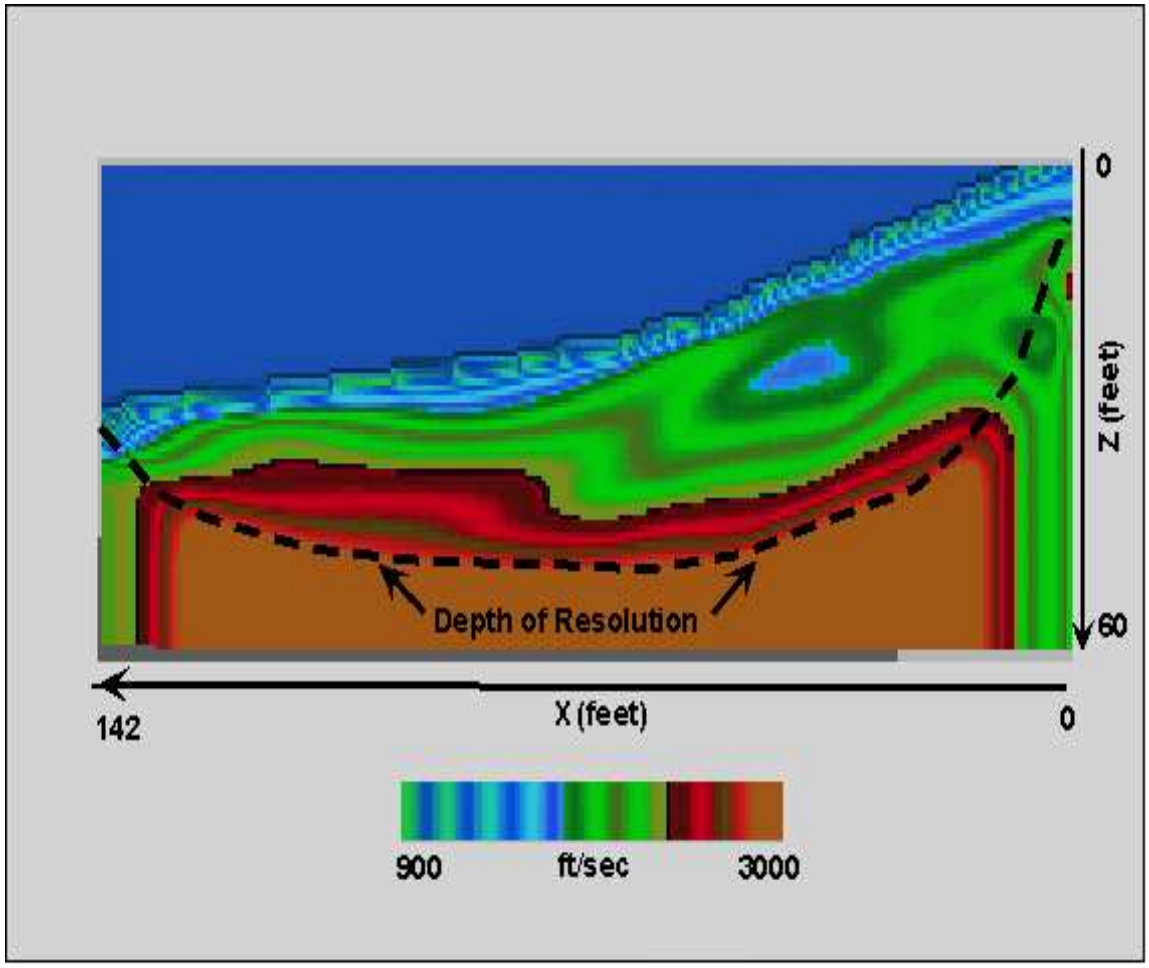

Figure 36: X-Z slice of the 3-D velocity tomogram sliced at y=15 ft.

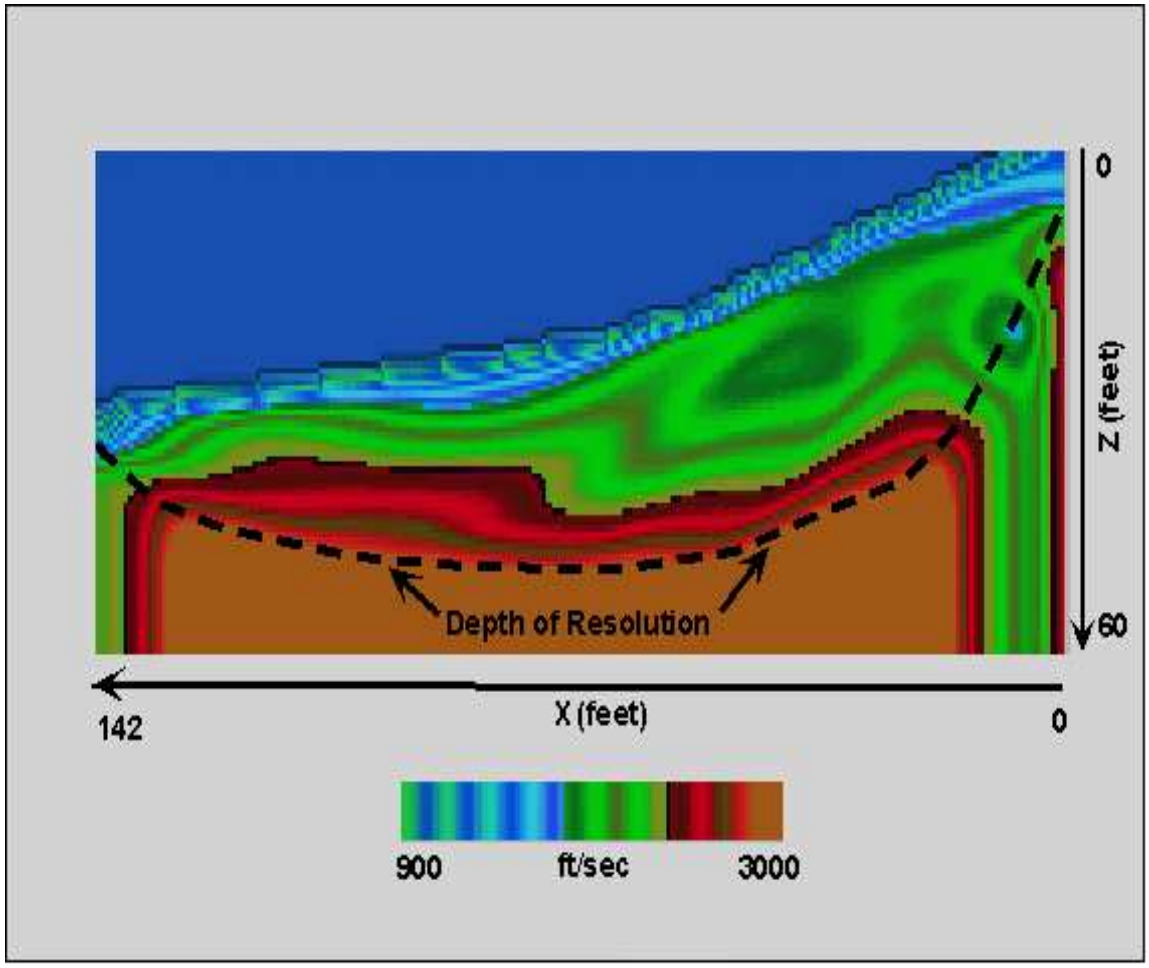

Figure 37: X-Z slice of the 3-D velocity tomogram sliced at y=20 ft.

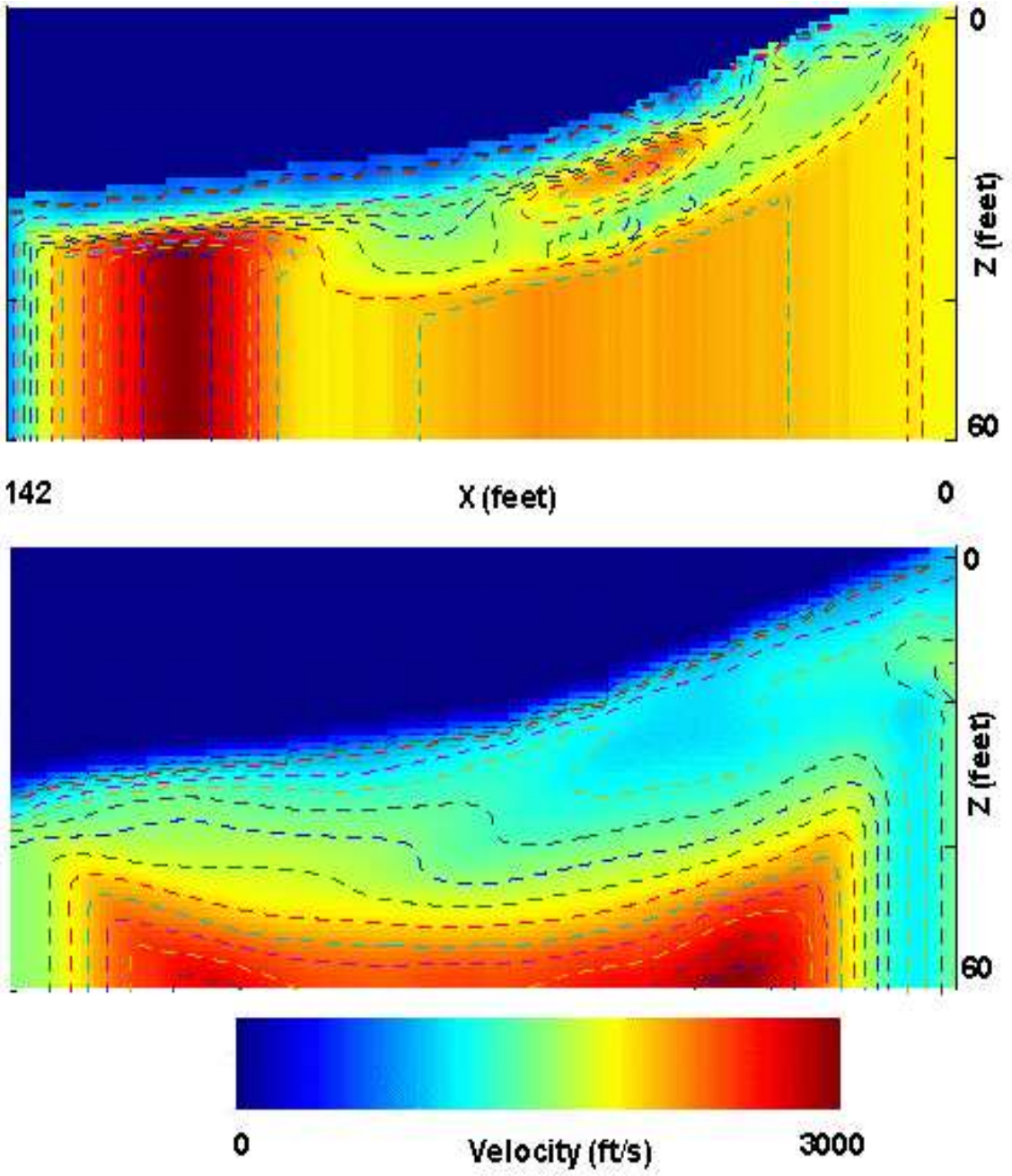

Figure 38: Comparison of 2-D vs 3-D tomograms. The colluvial wedge is more clearly defined in the 3-D tomogram (bottom) than in the 2-D tomgram (top).

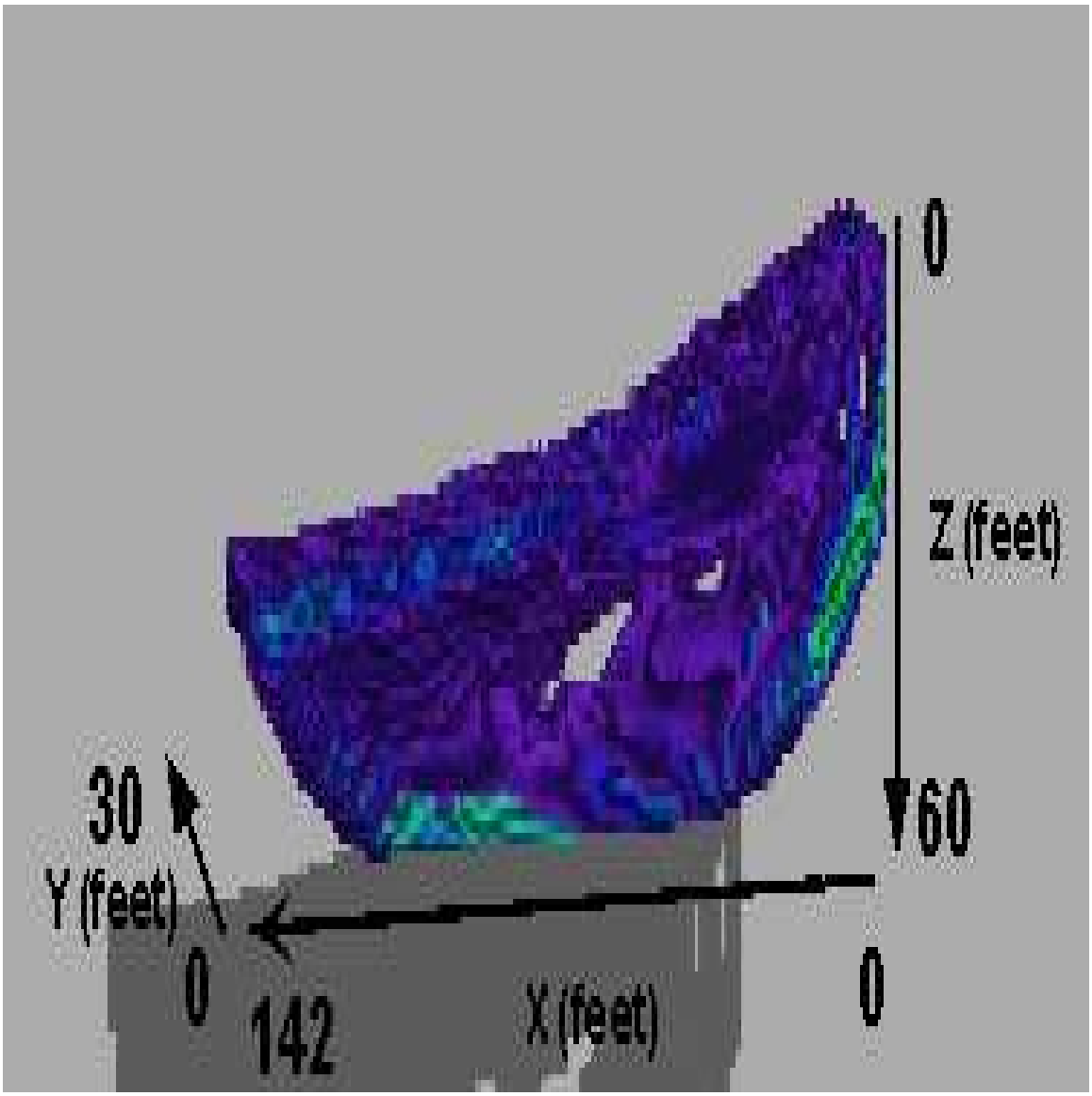

Figure 39: Images of raypaths showing areas that were visited by at least 500 rays.

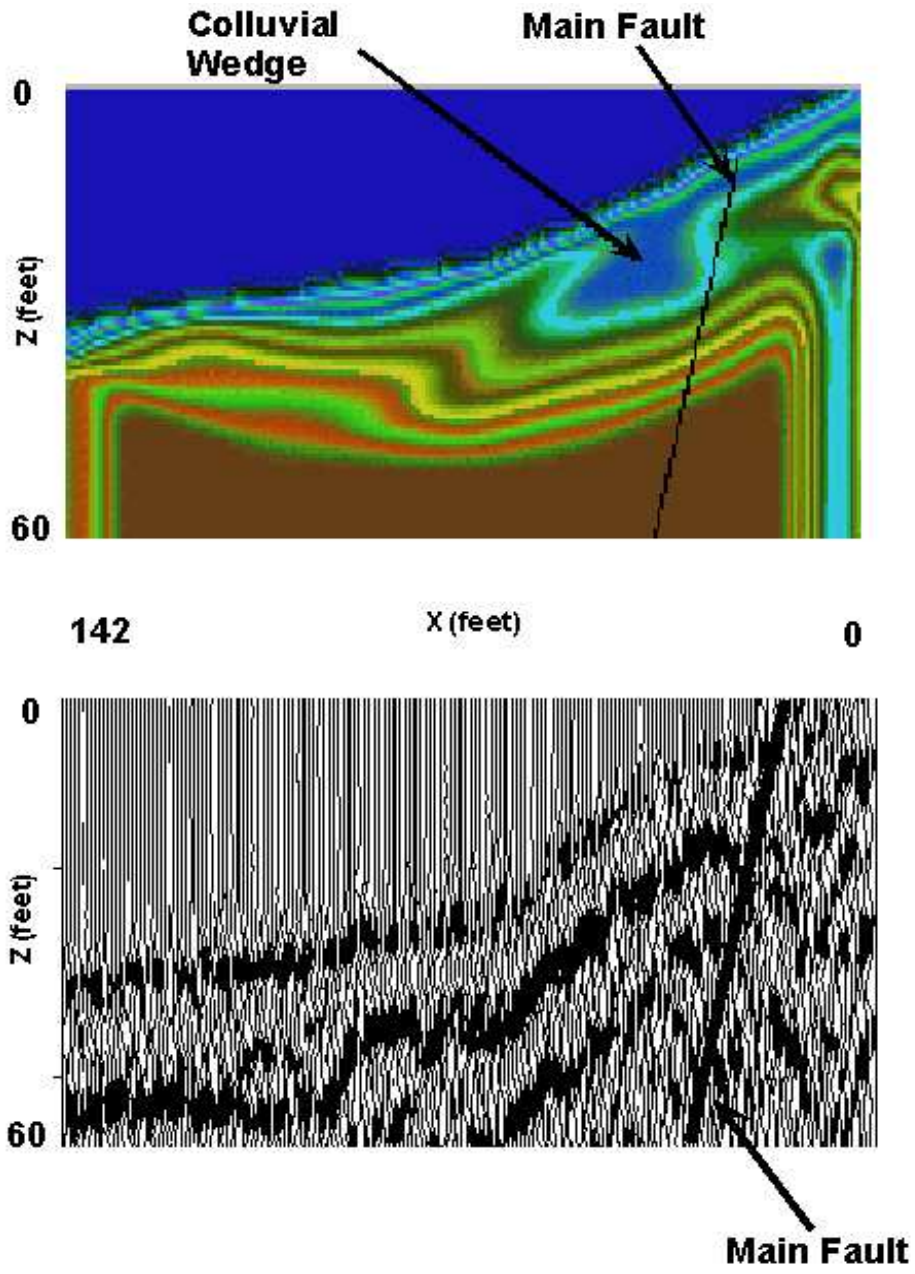

Figure 40: Comparison of the 3-D tomogram and the final stacked section. The colluvial wedge is clearly imaged in the tomogram, but its presence in the stacked section is ambiguous.

5. INTERPRETATION

The goal of this research was to use the resulting seismic images to deduce the paleoseismic history of the fault. Previously it was thought that seismic methods can only be useful in two ways: 1) detecting fault locations and 2) characterizing subsurface strata that have been offset, folded, or tilted by faulting (McCalpin, 1996). Several previous paleoseismic investigations have been successful in detecting fault locations and characterizing the subsurface strata (Crone and Harding, 1984; Miller and Steeples, 1986; Benson and Mustoe, 1991; Stephenson, 1993) but in these studies seismic methods were not able to clearly delineate the location and shape of colluvial wedges, and therefore could not determine the number or size of prehistoric earthquakes. The 3-D refraction traveltime tomography method used in this project is able to image a colluvial wedge and is therefore capable of providing information on the size of prehistoric vertical displacements.

5.1 Measuring Displacement From The Colluvial Wedge

Fault scarp degradation models suggest that scarp heights are typically twice the maximum thickness of the colluvial wedge if the slopes of offset beds are not too steep and the recurrence interval is not too short (Ostenaa, 1984). Thus, as a first approximation the initial scarp height of the most recent event on the Oquirrh fault is assumed to be twice the maximum thickness of the colluvial wedge. Measurements were made from X-Z slices of the 3-D tomogram at Y=10 ft, Y=15 ft, and Y=20 ft and the maximum thickness was measured at 11.4 ft. Since the colluvial wedge was identified in the 3-D tomogram as a region of low velocity, the thickness of the colluvial wedge was measured from the location where the vertical velocity gradient was zero on the top of the colluvial wedge to the point where the velocity gradient again reached

zero on the bottom of the colluvial wedge. Figure 41 shows the colluvial wedge at Y = 10 ft. The thickness of the colluvial wedge measured from the 3-D tomogram ranged from 11.4 ft to 9.5 ft compared to a range of 8.5 ft to 9.2 ft taken from the trenching studies (Olig et al., 1996).

5.2 Calculating Net Vertical Tectonic Displacement

Net vertical tectonic displacement is a measure of vertical slip across a fault caused by a surface-rupturing earthquake (Schwartz, 1988). Calculating the amount of vertical slip across a fault consists of three estimates: 1) displacement on the main fault, 2) tilt angle of strata over a certain distance, and 3) vertical displacement on the antithetic fault (McCalpin, 1996). The net vertical tectonic displacement, T_{net}, can be calculated by the following equation:

$$T_{net} = T_m - [(W tan\phi) + T_a]. \tag{7}$$

As shown in Figure 42, ϕ is the tilt angle of shallow strata over the horizontal distance W, T_m is the vertical displacement across the main fault, and T_a is the vertical component of displacement across the antithetic fault. This equation shows that T_{net} is the vertical displacement on the main fault minus the effects of tilting and antithetic faulting. The amount of vertical displacement, T_m, on the main fault is measured from Figure 41 to be $T_m = 22.8$ feet.

All other components, W, T_a, and ϕ in equation 7 are measured from the migrated section. The tilt angle ϕ is estimated by measuring the dip angle of horizon 1 both outside of the graben and inside the graben near the main fault. Outside of the graben horizon 1 dips 2° to the west; and inside the graben near the main fault, horizon 1 dips 2° to the east so the total amount of tilting on horizon 1 is $\phi = 4°$. This value is in good agreement with the 3° angle measured by Olig et al. (1996) from trench logs.

The inflection point of tilting is estimated at CMP 350 which implies tilting over a distance of $W = 169$ ft. The amount of displacement across the antithetic fault is measured on horizon 1 and is $T_a = 4.3$ feet. The location of these measurements can

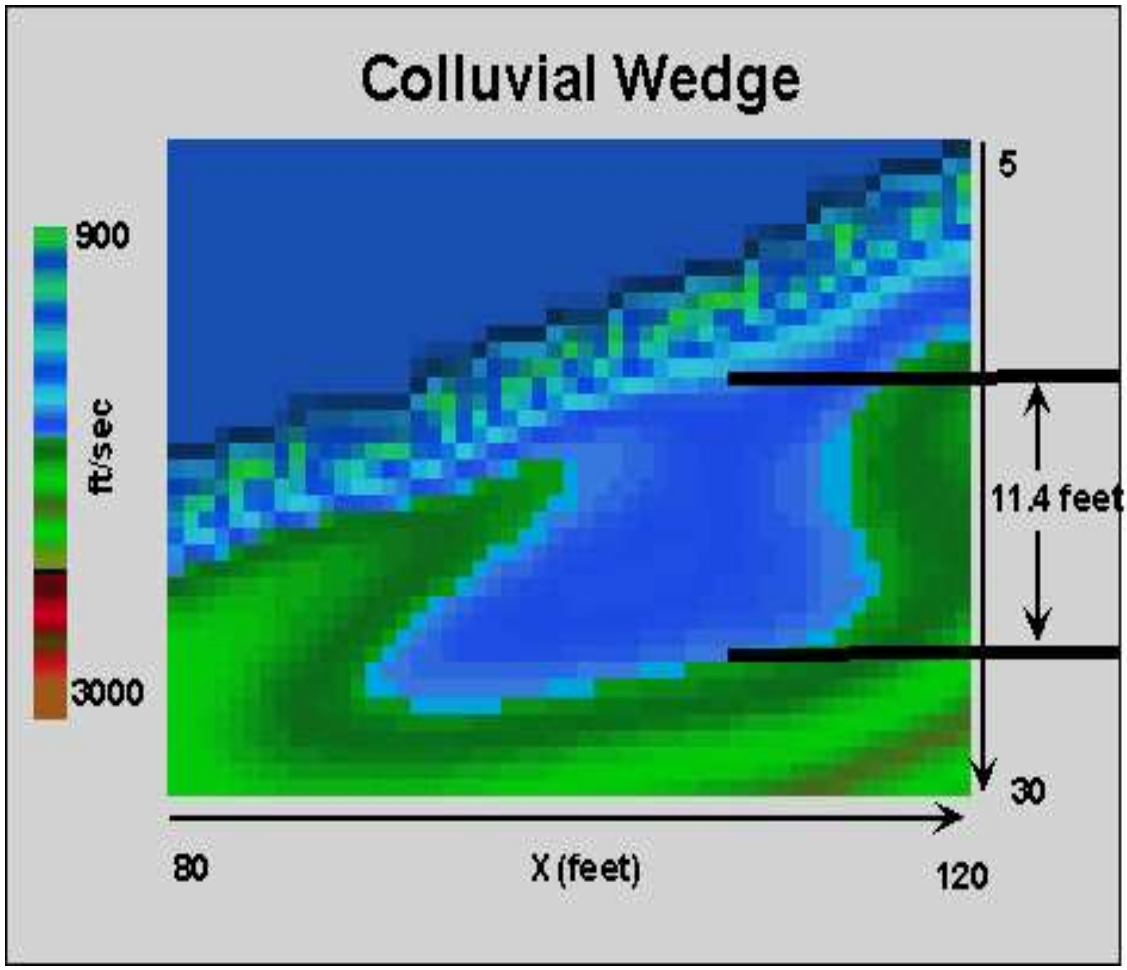

Figure 41: Image of the colluvial wedge showing where the maximum thickness was measured.

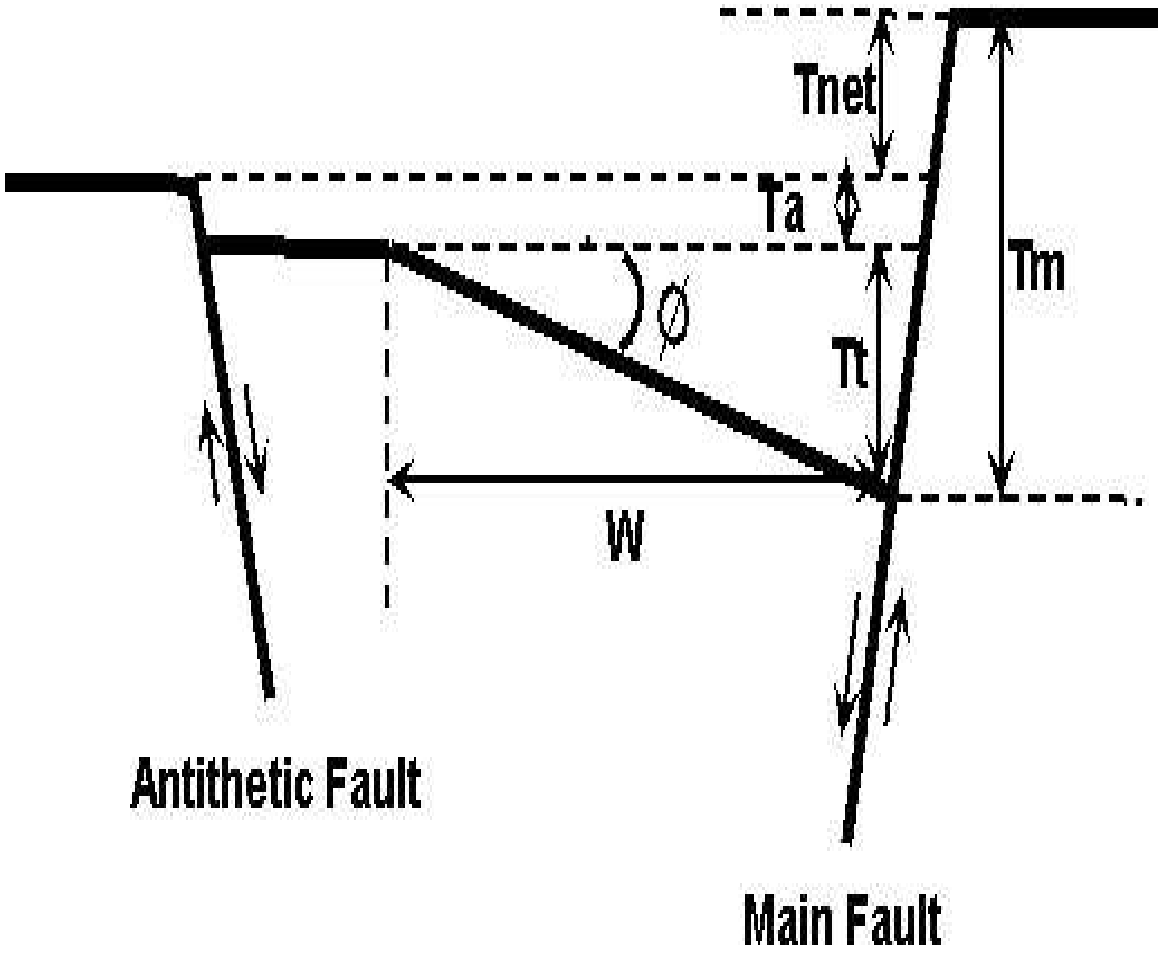

Figure 42: The components required for calculating net vertical tectonic displacement (T_{net}). The components are displacement (T_m), tilt displacement (T_t) over a certain distance (W), and vertical displacement on the antithetic fault (T_a).

be seen in Figure 43. Plugging these values into equation 7 gives an estimate of T_{net} = 6.7 feet for the net vertical tectonic displacement. In comparison, the trenching study of Olig et al. (1996) gives a "best estimate" of 7.2 ft for the net vertical tectonic displacement.

5.3 Calculating Paleoearthquake Magnitude

Although several types of evidence can be used to estimate the size of prehistoric earthquakes, inferring paleoearthquake magnitude from maximum displacement is a common practice (Wells and Coppersmith, 1994). In addition, the paleoearthquake magnitude can be inferred by the surface rupture length. For this investigation I calculate the magnitude of the most recent event on the Oquirrh fault using both pieces of evidence with emphasis on maximum displacement, where the magnitude estimate based on surface rupture length is mainly for comparison. Inferring paleoearthquake magnitude from surface rupture length can be misleading as it can be difficult to determine if the surface expression of a paleoearthquake is the result of a single event.

5.3.1 Calculating Paleoearthquake Magnitude From Displacement

The method of inferring paleoearthquake size from maximum displacement involves calculating the net vertical tectonic displacement T_{net} and comparing it with measurements from historic earthquakes (McCalpin, 1996). Compilations of historic earthquakes (Bonilla et al., 1984; Wells and Coppersmith, 1994) yield empirical relationships relating maximum displacement (MD) to moment magnitude (M) and surface rupture length (SRL) to moment magnitude. Wells and Coppersmith (1994) give a regression equation for normal faults relating MD to the moment magnitude:

$$M = 6.61 + 0.71 * log(MD), \tag{8}$$

where MD is given in meters. Plugging the parameters in Table 2 into this equation

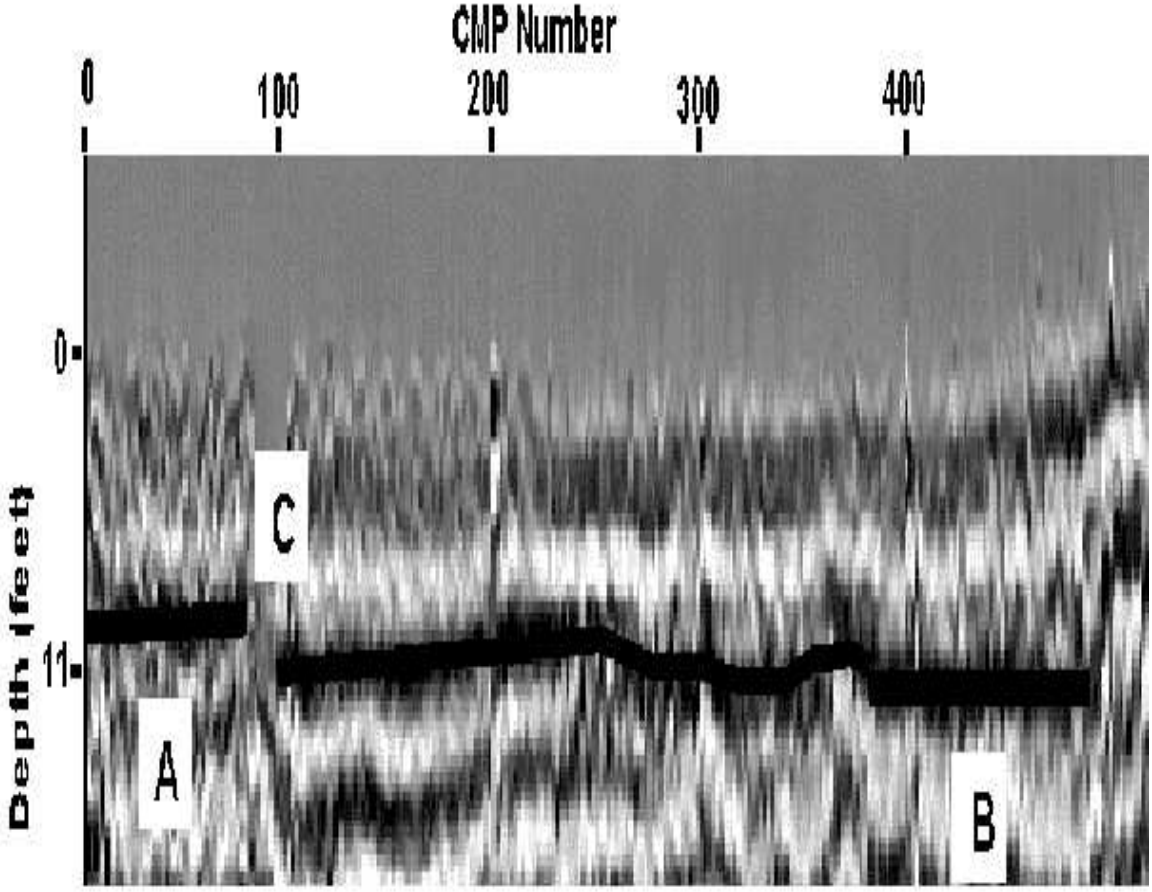

Figure 43: The amount of dip on horizon 1 is measured outside the graben at location A and inside the graben at B to define the amount of tilt due to faulting. Offset on the antithetic fault was measured at location C.

yields a moment magnitude of 6.8 for the most recent earthquake on the Oquirrh fault. This compares well with the Olig et al. (1996) estimate of 7.0 moment magnitude.

5.3.2 Calculating Paleoearthquake Magnitude From Surface Rupture Length

The method of inferring paleoearthquake magnitude from surface rupture length involves measuring the surface rupture length and comparing this value with measurements from historic earthquakes (McCalpin, 1996). Wells and Coppersmith give an empirical equation for normal faults relating M and SRL:

$$M = 4.86 + 1.32 * log(SRL), \tag{9}$$

where SRL is given in kilometers. Soloman (1996) measureed the straight line length of the Oquirrh fault at 21 km. Using an SRL of 21 km yields an estimate of 6.6 for the moment magnitude. This estimate of moment magnitude is less than the estimate from displacement, but is in agreement with the claim by Mason and Smith (1993) that estimates based on displacements are generally 20 % higher than estimates based on rupture length for Quaternary faults in the Intermountain Seismic Belt.

Table 2. Parameters used to calculate paleoearthquake magnitude.

Source	3-D Tomogram	Migrated Seismic Section
Wedge Thickness	11.4 ft	
Vertical Displacement of Main Fault	22.8 ft	
Tilt Angle of Horizon 1		4°
Distance Between Inflection Point and Main Fault		169 ft
Vertical Displacement (antithetic fault)		4.3 ft
Dip on Main Fault		85°±10°
Dip on Antithetic Fault		75°±10°
Paleoearthquake Magnitude Estimate	6.8	6.8

Mason (1992) suggested that a straight-line measurement of SRL tended to underestimate fault dimensions while maximum displacements on normal faults tended to overestimate displacement due to graben formation and back tilting. This suggests that these two parameters may counterbalance each other to give a more accurate estimate of paleoearthquake magnitude.

5.3.3 Calculating Paleoearthquake Magnitude From Displacement and Surface Rupture Length

The method of inferring paleoearthquake magnitude from displacement and surface rupture length involves measuring MD and SRL and comparing these values with measurements from historic earthquakes (McCalpin, 1996). Mason and Smith (1993) present an empirical equation relating MD and SRL to surface wave magnitude (M_s):

$$M_s = 6.1 + 0.47 * log(MD * SRL), \tag{10}$$

where MD is in meters and SRL is in kilometers. Using the previously calculated 6.7 ft for MD and 21 km (Soloman, 1996) for SRL yields a estimate for M_s of 6.9. Bonilla et al. (1984) give empirical equations relating M_s to MD and SRL:

$$M_s = 6.98 + 0.742 * log(MD), \tag{11}$$

and

$$M_s = 5.17 + 1.237 * log(SRL). \tag{12}$$

Using MD = 2.0 m yields an estimate for M_s of 7.2, and using SRL = 21 km yields an estimate for M_s of 6.8. This does support the claim by Mason (1992) that MD and SRL may counterbalance each other to give a more accurate estimate of the paleoearthquake magnitude. The estimate of M_s using both parameters falls between the estimates using each parameter independently.

There are limitations involved with conducting paleoseismology investigations of

this type. Measuring displacement from the 3-D tomogram is not able to account for oblique-slip. It is also possible that the location of the seismic survey is not coincident with the location of maximum displacement on the fault, although the survey area is located in the central region of the scarp, where displacements are usually large (McCalpin, 1996). The 3-D survey also provides multiple measurements and can, therefore, have a better chance of finding the maximum displacement. There is also the possibility that the empirical relationships between historic earthquakes and the Oquirrh fault does not fit, although there is no available evidence that this is the case.